THE JOURNAL OF PHYSICAL CHEMISTRY C
A JOURNAL OF THE AMERICAN CHEMICAL SOCIETY

pubs.acs.org/JPCC

Article

Stability of Pt Skin Intermetallic Core Catalysts and Adsorption Properties for the Oxygen Reduction Reaction

Seong Kyu Kim, Kihyun Shin, and Graeme Henkelman*

Cite This: J. Phys. Chem. C 2021, 125, 3527−3534

Read Online

ACCESS | Metrics & More | Article Recommendations | Supporting Information

ABSTRACT: Density functional theory calculations were used to determine the stability of metal slabs consisting of a Pt surface monolayer and intermetallic supporting layers made from combinations of six transition metal elements (Pt, Fe, Co, Ni, Cu, and Ag), as a model system for Pt skin intermetallic core nanoparticle catalysts. The stability of the slabs is largely determined by strain at the interface of the Pt skin and the subsurface intermetallic, which was described by a lattice matching parameter (r). The surface charge on the Pt skin was found to be correlated with the average electronegativity (EN) of the intermetallic core, so this average EN was used as a descriptor for how the electronic coupling (or ligand effect) affects adsorption energies. A total of 46 slabs were investigated in terms of their stability, from which 10 stable slabs were selected for further studies of adsorbate binding (OOH*, O*, and OH*) that are intermediates in the oxygen reduction reaction (ORR). The correlation between all three adsorption energies and descriptors r and EN was found. Using a linear fit between our descriptors and the calculated adsorption energies, the overpotential for the ORR was obtained as a function of r and EN, from which a volcano plot was produced. The volcano peak was found at r = 0.96 or at EN = 2.025. Interestingly, neither r nor EN was a sufficient single reactivity descriptor as the data points were well off the general trend in both linear fits; this implies that both the strain effect and the ligand effect influence the adsorption energies, although they are partly correlated. The (r, EN) target peak parameters were used to screen over 241 intermetallic combinations of transition metal elements as active ORR activity. This analysis identified 11 intermetallic compounds which can support a Pt skin to have a high predicted ORR activity.

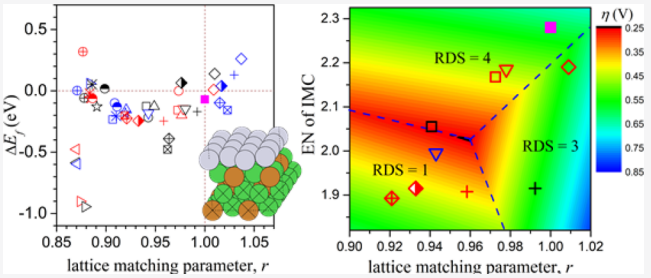

INTRODUCTION

Pt-based catalysts have many industrial applications. In fuels, they work as an essential component to generate electricity through electrochemical conversion[1−4] of oxygen and hydrogen in aqueous medium. In this application, the oxygen reduction reaction (ORR)[5−10] occurring at the cathode is known to be rate-determining. Besides the rate of the ORR, there are many other aspects to improve the efficiency of catalysts for fuel cells: the overpotential, electrode stability, electrolyte effects, and cost of Pt. The ORR process on a Pt-based catalyst is intrinsically complicated and has been understood with many suggested mechanisms. The validity of the suggested mechanisms has been tested using computational studies based on density functional theory (DFT), as they can provide useful information on the thermodynamic stability of catalysts themselves as well as intermediates along the reaction pathways.[11−14]

An attractive form of Pt-based catalysts is the core−shell nanoparticle (NP), in which the adsorption characteristics of Pt in the shell can be modified by metal elements in the core. When the core is composed of metals with a simple ratio of elemental composition, it can form a stable intermetallic-ordered phase. In such a structure, the thermodynamic states of intermediate adsorbates in a catalytic pathway can be varied by tailoring the composition in the core. Additionally, the amount of expensive Pt can be reduced by limiting it to the shell. Modification of adsorbate states on the shell can be achieved by a strain induced by lattice mismatch (strain effect)[15−19] or electronic coupling between the core and shell (ligand effect).[20−22] The strain and ligand effects are expected to be greatest when the shell is just one monolayer thick. For this structure, we will use the term "Pt skin intermetallic core (IMC)" and denote it as IMC@Pt.

Understanding how the catalytic properties are influenced by the elements in the core necessitates studies at the atomic scale. Although DFT has been employed for a wide variety of catalytic processes, current DFT calculations are limited to systems with a few hundreds of atoms or NPs smaller than about 3 nm in diameter. In contrast, many catalytic NPs have been produced with diameters larger than 5 nm. For such large

Received: October 26, 2020
Revised: January 20, 2021
Published: February 4, 2021

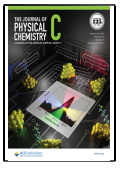

particles, a slab model can provide the essential information regarding their catalytic properties, ignoring small size confinement effects.

In this work, we first investigate the stabilities of IMC@Pt slabs composed of combinations of six transition metal elements (Pt, Fe, Co, Ni, Cu, and Ag)[23−25] and then study the adsorption properties of ORR intermediates on selected catalysts. Specifically, we focus on two macroscopic parameters to describe the adsorption energies: a lattice matching parameter and the average electronegativity (EN) of Pauling's scale,[26] which represent the strain and ligand effects, respectively.

METHODS

The primary tool used in this work is DFT calculations based on the projector-augmented wave[27] method and the revised Perdew−Burke−Ernzerhof functional,[28] as provided by the Vienna Ab initio Simulation Package.[29] Details of the calculation methods are described in the Supporting Information.

This work is divided into two parts. In the first part, the stability of IMC@Pt NPs was investigated. In the second part, the adsorbed states of ORR intermediates on several IMC@Pt NP candidates suggested by the first part were investigated. The slab models of IMC@Pt were constructed with 16 Pt atoms in the first layer and 3 × 16 IMC atoms in the second through fourth layers. Combinations of Pt, Fe, Co, Ni, Cu, and Ag with elemental ratios of 3:1 or 1:1 made up the IMCs. The chemical stability of these IMCs was not considered at this stage. The crystal structures of the IMCs were obtained from the Materials Project database,[30] excluding those that do not accommodate a Pt(111) structure on the surface; these were re-optimized to find their optimal lattice constants. The re-optimized lattice constants for the bulk IMCs were applied to the Pt skin layer; therefore, the Pt skin layer was subjected to a lattice mismatch with respect to a (111) surface of bulk Pt. When optimizing the slabs and adsorbates on the slabs, atoms in the first and second layers were relaxed, while atoms in the third and fourth layers were fixed, unless stated otherwise. Further details of the slab preparation are provided in the Supporting Information. To quantify the stability of IMC@Pt, we define the formation energy as

$$\Delta E_f = [E(\text{IMC@Pt}) - E(\text{IMC})]/16 - E(\text{Pt}) \quad (1)$$

where E(IMC@Pt) is the energy of the optimized IMC@Pt, E(IMC) is the energy of the IMC slab, and E(Pt) is the energy of a Pt atom in the bulk. The division by 16 is needed, as there are 16 atoms per layer. Additionally, the adhesion energy of IMC@Pt is defined as

$$\Delta E_{adh} = [E(\text{IMC@Pt}) - E(\text{IMC}) - E_{skin}]/16 \quad (2)$$

where E_{skin} is the energy of the unsupported Pt skin layer that was lifted off the prepared IMC@Pt. Note that the geometry of the unsupported Pt skin is perfectly flat; relaxation did not occur because of the high symmetry. The difference between ΔE_f and ΔE_{adh} is the formation energy of the Pt skin layer

$$\Delta E_{skin} = \Delta E_f - \Delta E_{adh} = E_{skin}/16 - E(\text{Pt}) \quad (3)$$

Once stable slabs were found in the first part of our work, adsorbate binding energies were calculated in the second part to determine their catalytic properties. The following 4e$^-$ pathway has been considered the likely mechanism for the ORR process in acidic media: $O_2(g) + 4H^+(aq) + 4e^- \rightarrow 2H_2O(l)$.

$$O_2(g) + H^+(aq) + * + e^- \rightarrow OOH^* \text{ (step 1)}$$

$$OOH^* + H^+(aq) + e^- \rightarrow O^* + H_2O(l) \text{ (step 2)}$$

$$O^* + H^+(aq) + e^- \rightarrow OH^* \text{ (step 3)}$$

$$OH^* + H^+(aq) + e^- \rightarrow H_2O(l) \text{ (step 4)}$$

Here, * denotes an adsorption site and O*, OH*, and OOH* are the adsorbed species. In calculating the energy changes in steps 1−4, a few species can be replaced by computationally compatible ones. Following a simple model suggested by Nørskov et al.,[31−33] $H^+(aq) + e^-$ under no bias voltage can be replaced by $1/2H_2(g)$, assuming that the reference electrode is the standard hydrogen electrode (SHE) and $H_2O(l)$ can be replaced by H_2O(g, 0.035 bar). At the equilibrium voltage of 1.23 V, $O_2(g) + 2H_2(g)$ can be replaced by $2H_2O(l)$. Therefore, disregarding the bias, these replacements modify steps 1−3 to the following equations of reactions 4−6.

$$2H_2O(g) + * \rightarrow OOH^* + \frac{3}{2}H_2(g) \quad (4)$$

$$H_2O(g) + * \rightarrow OH^* + \frac{1}{2}H_2(g) \quad (5)$$

$$H_2O(g) + * \rightarrow O^* + H_2(g) \quad (6)$$

Thus, the adsorption energies of O*, OH*, and OOH* are defined as follows

$$\Delta E_{ads}(OOH^*) = E(OOH^*) + \frac{3}{2}E(H_2) - 2E(H_2O) - E(*) \quad (7)$$

$$\Delta E_{ads}(O^*) = E(O^*) + E(H_2) - E(H_2O) - E(*) \quad (8)$$

$$\Delta E_{ads}(OH^*) = E(OH^*) + \frac{1}{2}E(H_2) - E(H_2O) - E(*) \quad (9)$$

In converting the computed energy (E) of each species to its free energy (G), contributions of zero-point energy (ZPE) and the entropy term (-TS) are added. While the ZPEs can be obtained from a vibrational frequency analysis, we used the values for the entropy contribution suggested by Nørskov et al.[31] To compensate for the difference between the isolated adsorbate in our calculations and the solvated adsorbate in aqueous medium, the solvation energies for the three adsorbates were also added. For this, we adopted the values calculated by Liu et al.[34] for the adsorbates in three bilayers of water; they were −0.58, −0.04, and −0.79 eV for OOH*(aq), O*(aq), and OH*(aq), respectively.

Then, free energy changes for steps 1−4 can be written as

$$\Delta G_1(0) = \Delta G_{ads}(OOH^*) + 4 \times 1.23 \text{ eV} \quad (10)$$

$$\Delta G_2(0) = \Delta G_{ads}(O^*) - \Delta G_{ads}(OOH^*) \quad (11)$$

$$\Delta G_3(0) = \Delta G_{ads}(OH^*) - \Delta G_{ads}(O^*) \quad (12)$$

$$\Delta G_4(0) = -\Delta G_{ads}(OH^*) \quad (13)$$

Here, ΔG_{ads} for each adsorbate includes the correction terms mentioned above.

https://dx.doi.org/10.1021/acs.jpcc.0c09674
J. Phys. Chem. C 2021, 125, 3527−3534

RESULTS

Stability of IMC@Pt Slabs. The calculated values of ΔE_f, ΔE_{adh}, and ΔE_{skin} for 46 IMC@Pt slabs are plotted against the lattice matching parameter (r) in Figure 1. The list of catalysts

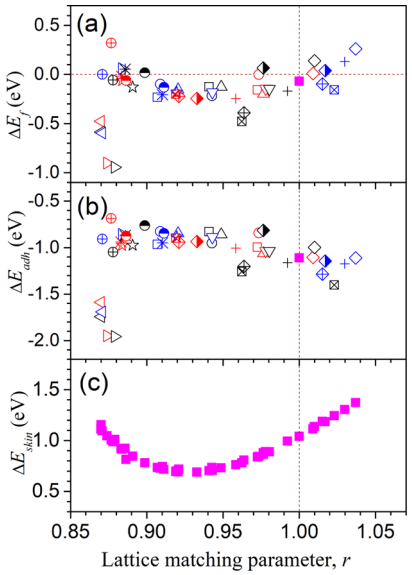

Figure 1. Values of ΔE_f, ΔE_{adh}, and ΔE_{skin} plotted against lattice matching parameter (r). The caption for plot symbols is shown in Scheme 1.

and their corresponding plot symbols are shown in Scheme 1. The lattice matching parameter is given by the optimized lattice constant of bulk IMC divided by that of Pt (3.991 Å).

In general, for slabs with r values less than 0.88, the ΔE_f and ΔE_{adh} values deviate largely from the general trends. The negative deviations of this kind are a result of high strain on the skin layer. The skin layer in the optimized structures of this kind was found to be partially peeled off to form an aggregated cluster of Pt atoms. This phenomenon is shown in Figure 2a, in which the root-mean-square deviations (RMSDs) of the z-coordinates of the Pt skin atoms were plotted. In contrast, the Pt atoms remained epitaxial on the surface when r was greater than 0.90; therefore, r = 0.90 was determined to be the lower limit for the stable slab.

For slabs with r greater than 0.88, the ΔE_f values follow an asymmetric curve. If ΔE_f (Figure 1a) is decomposed into ΔE_{adh}(Figure 1b) and ΔE_{skin} (Figure 1c), we can see that ΔE_{skin} is the primary contributor to the curved trend, while ΔE_{adh} contributes a slightly negative slope when plotted against r. The formation energy (ΔE_f) is negative when r is between 0.90 and 1.00; therefore, IMC@Pt structures within this range are considered to be stable. The value of r that minimizes ΔE_f is difficult to determine because of scatter in the data, but it can be determined more easily from the ΔE_{skin} values. The r

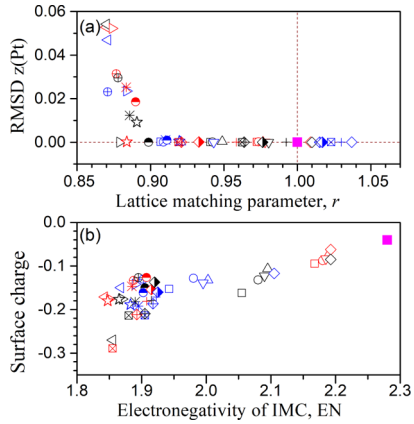

Figure 2. RMSDs of z-coordinates and surface charge of the skin Pt atoms. The legend for the plot symbols is shown in Scheme 1.

value that minimizes ΔE_{skin} is 0.925 ± 0.005. At the corresponding lattice constant of 3.924 Å, a monolayer of Pt atoms in the (111) orientation is most stable.

When r decreases, the increased compressive strain shifts down the surface d-band.[15,16] The increase of the adhesion energy (ΔE_{adh}) at decreasing r in the stable region shown in Figure 1b implies that the downshift for IMC@Pt is less than that for IMC. The dependence appears linear with r, which suggests that the lattice matching parameter is a good macroscopic parameter to quantify the strain effect.

The ligand effect on the adsorbed states is the result of electronic coupling between surface and subsurface atoms, which induces polarization on the surface layer. To elucidate this effect, the charge on each atom in the slab was obtained with a Bader analysis.[35] The surface charge of a Pt atom in a pure Pt slab was found to be −0.041, while those of all IMC@Pt were more negative. First, we plotted the average charge of the Pt skin atoms against r, but no apparent correlation was found (shown in Supporting Information, Figure S3a), confirming that the strain does not systematically influence the surface charge. However, when the surface charge was plotted against the weighted average EN of the IMC, a weakly linear dependency was found, as shown in Figure 2b. The majority of the scattered data of the linear dependency comes from unstable slabs with r less than 0.9; the linear dependency would be clearer if those data were removed (shown in Supporting Information, Figure S3b). Based on this correlation, we used the average EN of the IMC as a macroscopic parameter to quantify the ligand effect.

Adsorption on Selected Slabs. In the first part of this work, we found that r is a good macroscopic parameter to judge the stability of IMC@Pt structures due to the strain effect, and the average EN is a good macroscopic parameter to quantify the ligand effect upon adsorbate formation because it is weakly correlated with the surface charge of the slab. In this

Scheme 1. List of IMC@Pt in This Work and Their Corresponding Plot Symbols

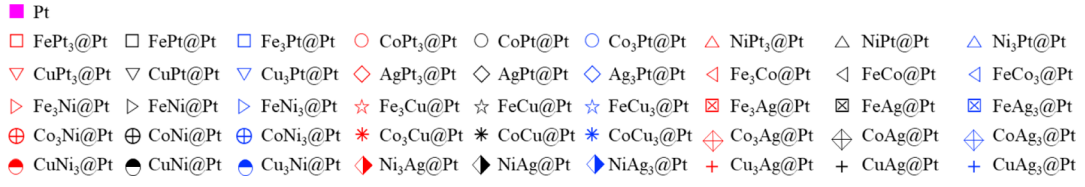

https://dx.doi.org/10.1021/acs.jpcc.0c09674
J. Phys. Chem. C 2021, 125, 3527−3534

second part, we investigate the adsorption properties of selected stable slabs.

In selecting slabs, the following three factors were considered for ease of subsequent analysis. (1) The lattice matching constant r should be between 0.90 and 1.01 to be in the stable region. (2) The EN of the IMC should span the entire range more or less evenly. (3) The lattice structure should be either face-centered cubic (fcc) or face-centered tetragonal because a subsurface layer cut from a hexagonal or rhombohedral IMC exhibits two domains of different metals which generate additional complexity. Considering these three factors, we selected the following catalysts to be investigated for the adsorption properties for ORR: $FePt_3$@Pt, FePt@Pt, $CuPt_3$@Pt, Cu_3Pt@Pt, Co_3Ag@Pt, Cu_3Ag@Pt, CuAg@Pt, $AgPt_3$@Pt, and Ni_3Ag@Pt. The nine catalysts have either Pt or Ag in the IMC; this is because Ag is the only element, among the transition metal elements in this work, which is large in size and has a smaller EN than Pt.

O adsorbs at the three-fold hollow site of the Pt(111) surface, while OH or OOH adsorbs on top of a Pt atom of the (111) surface. In all the selected slabs, there are two kinds of adsorption sites depending on the bimetallic composition in the subsurface layer closet to the adsorption site. The adsorption energies of the two sites are different. However, we will present only the data for the lower energy states, and the data for both adsorption sites are given in Supporting Information. This selection does not change the results of this paper.

In Figure 3a, the adsorption energies calculated using 7 are shown as a function of r. The adsorption energies appear to

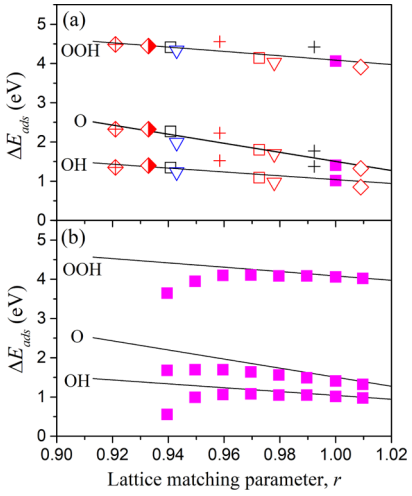

Figure 3. Adsorption energies plotted against lattice matching parameter (r). The plot symbols are defined in Scheme 1. (a) Adsorption energies for the 10 slabs are plotted. Least square fit lines for the data are drawn for visual guidance. (b) Adsorption energies for a pure Pt slab with varied lattice constants are plotted. The same three lines in (a) are drawn in (b) to show visual guidance.

decrease linearly with increasing r; however, the linear dependency is not perfect. The adsorption energies for CuAg@Pt (black plus symbol) and Cu_3Ag@Pt (red plus symbol) deviate slightly from the linear trend of other catalysts. Overall, the linear fits for OH and OOH are worse than that for O because of the deviations of these two catalysts.

To understand if the strain effect due to the lattice mismatch is the dominant factor for the pseudolinear dependency shown in Figure 3a, we calculated the adsorption energies for pure Pt(111) slabs with varied lattice constants and plotted them against r, as shown in Figure 3b. They deviate severely from the linear lines of Figure 3a, especially when r is below 0.95, where the distortions in the adsorption geometries are apparent. For example, in the adsorption geometries of OH on Pt(111) with r below 0.95, the Pt skin atom that OH is adsorbed to is lifted up significantly. As shown in Figure 1c, the Pt skin layer supported on stable IMCs is most stable at an r value of 0.925; however, Figure 3b shows that when the Pt skin is loaded onto the Pt core at this r, a part of the skin layer is unstable, likely because the supporting layers are unstable.

Additional calculations were done for adsorption energies on two series of theoretical Pt slabs. The data of these calculations are shown in Supporting Information (Table S6). In one series of theoretical Pt slabs, the lattice constant was varied only laterally, while the lattice constant along the vertical direction was maintained the same as that of bulk Pt (3.991 Å). The adsorption energies of this series turned out to be nearly same as those in Figure 3b. In the other series of theoretical Pt slabs, the lattice constant was varied only vertically, while the lateral lattice constant was constrained to that of bulk Pt. The adsorption energies of this series turned out to be nearly the same as that of the Pt(111) slab with the lattice matching parameter of one. These two trends suggest that the adsorption energies are not sensitive to the vertical stress produced by the supporting layers but instead depend on the interatomic distance in the Pt skin layer.

In Figure 4, the same adsorption energies in Figure 3a are plotted against the average EN of the IMC atoms. The plot

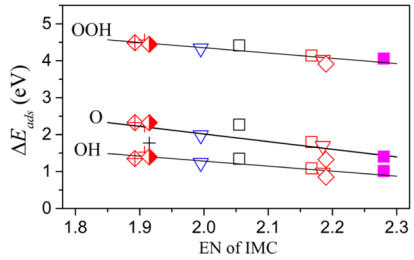

Figure 4. Adsorption energies plotted against the average EN of the IMC. The plot symbols are shown in Scheme 1. The three lines represent the least square fits for the data.

symbols appear to follow straight lines; however, a few data points (e.g., ΔE_{ads}(O) of CuAg@Pt) deviate from this trend. As a whole, we cannot conclude that average EN is a better macroscopic parameter than r for the dependency of the adsorption energies. In addition, we calculated the adsorption energies for several catalysts ($CuPt_3$@Pt, Cu_3Pt@Pt, Cu_3Ag@Pt, CuAg@Pt, and $AgPt_3$@Pt) with their lattice atoms fixed with the fcc lattice constant of Pt. The motivation for this calculation was to know whether the adsorption energies change significantly from the values with their lattice atoms relaxed, that is, if the average EN is the dominant factor or if they are close to those of Pt(111) when the lattice atoms are fixed with r = 1, that is, if r is the dominant factor. The result of this calculation, which is detailed in Supporting Information (Table S5), shows that the answer to which macroscopic factors are dominant is not conclusive.

https://dx.doi.org/10.1021/acs.jpcc.0c09674
J. Phys. Chem. C 2021, 125, 3527−3534

DISCUSSION

Strain Effect or Ligand Effect. The effects of strain and ligand on the adsorption energies have been investigated for numerous bimetal surfaces.[15−22] Following the studies so far, both effects are induced by shifts of the surface d-band, which is related to an interatomic matrix element V_{12} that describes the bonding between two neighboring atoms 1 and 2. According to Kitchin et al.,[20] V_{12} can be expressed as

$$V_{12} \propto \frac{(r_d^{(1)} r_d^{(2)})^{3/2}}{{d_{12}}^5} \quad (14)$$

where d_{12} is the interatomic distance between 1 and 2, and $r_d^{(j)}$ is a characteristic length that is related to the spatial extent of d-orbital of metal atom j. $r_d^{(j)}$ is proportional to the linear muffin-tin orbital potential parameters of j;[36,37] therefore, the numerator of eq 14 pertains to the ligand effect. In contrast, the interatomic distance d_{12} in the denominator of eq 14 pertains to the strain effect.

When the atomic size decreases, d_{12} decreases and $r_d^{(j)}$ also decreases in most transition metals. Therefore, the ligand effect and the strain effect are not independent but cumulative. This trend is also found in the relationship between the atomic size and the EN of transition metal atoms in this work. They vary in a parallel fashion, except that Ag is larger but its EN is smaller than that of Pt. Therefore, it is not surprising that both plots of the adsorption energies in Figures 3a and 4 show pseudolinearity with only a few data points off the linear trends. To be more specific, the O-adsorption energies are better correlated with the lattice matching parameter r, whereas the OH- and OOH-adsorption energies are better correlated with the average EN of the IMC. Additionally, the adsorption energy differences between the two adsorption sites (shown in Table S4 and Figure S3) are larger for O-adsorption than for OH- or OOH-adsorption. This difference perhaps reflects the different (three-fold hollow and on-top) adsorption geometries for the two adsorbates.

Thermodynamic View. Under no bias, the free energy changes shown in 10 are all negative, meaning that each of the four steps is spontaneous. Assuming that the ORR rate is thermodynamically controlled, the step with the least negative value of $\Delta G_i(0)$ is the rate-determining step (RDS). However, in an electrolyte cell, a potential can be applied to the exact energy from the reaction. Under a bias, the free energy of each step is

$$\Delta G_i(U) = \Delta G_i(0) + eU \quad (15)$$

where e is the magnitude of electron charge, U is the bias voltage, and i = 1, 2, 3, 4. In order for every step to be spontaneous, eU must be less than the absolute value of $\Delta G_i(0)$ for the RDS. As a measure of the efficiency of the catalyst, the overpotential (η) is defined as the overall free energy change minus the maximum bias potential (U_{max}).

$$\eta = 1.23\ \text{V} - U_{max} = 1.23\ \text{V} - \min[-\Delta G_i(0)/|e|],\ i = 1,\ 2,\ 3,\ 4 \quad (16)$$

$\Delta G_i(0)$, RDS, and η calculated with the data of 10 catalysts are shown in Table 1. The overpotential of Pt was calculated to be 0.58 V. In developing Pt-based catalysts, much effort has been extended to find catalysts with a lower η than this value. The RDS for the Pt-catalyzed ORR is step 3, in which O* is hydrolyzed to OH*. Therefore, in order for η to be lower, a catalyst should bind O more weakly and OH more strongly than Pt. This is, in general, not possible because the adsorption energies O* and OH* are positively correlated as shown in Figures 3 and 4. However, the adsorption energies of O* change more rapidly than those of OH* when they are plotted against r or EN, as shown in Figures 3 or 4. This results in lower values of η or switches to other RDS for most of the catalysts considered in this work.

Table 1. Free Energy Changes at Zero Bias ($\Delta G_1(0) - \Delta G_4(0)$ in eV), the RDS, and the Overpotential (η in V)

catalyst	$\Delta G_1(0)$	$\Delta G_2(0)$	$\Delta G_3(0)$	$\Delta G_4(0)$	RDS	η
Pt	−1.25	−2.27	−0.65	−0.75	3	0.58
$FePt_3$@Pt	−1.17	−1.96	−0.98	−0.82	4	0.41
FePt@Pt	−0.89	−1.77	−1.19	−1.08	1	0.34
Co_3Ag@Pt	−0.82	−1.78	−1.24	−1.09	1	0.41
$CuPt_3$@Pt	−1.28	−1.95	−0.99	−0.71	4	0.52
Cu_3Pt@Pt	−0.97	−1.97	−1.01	−0.97	1 or 4	0.26
Cu_3Ag@Pt	−0.75	−1.95	−0.97	−1.26	1	0.48
AgCu@Pt	−0.88	−2.27	−0.66	−1.11	3	0.57
$AgPt_3$@Pt	−1.39	−2.20	−0.74	−0.59	4	0.64
Ni_3Ag@Pt	−0.86	−1.78	−1.19	−1.13	1	0.37

Reactivity Descriptor. As a measure of the ORR activity, $-\eta$ is often plotted against the adsorption energy of an intermediate adsorbate as a reactivity descriptor.[38] The plot was projected to a peak of a volcano curve, from which the reactivity descriptor for the most efficient catalyst is predicted. However, in order to know the value of the reactivity descriptor in this scheme, the adsorption energies for a given catalyst should be computed accurately. Using a macroscopic parameter as a reactivity descriptor, if it is good enough, is a more straightforward approach. In this sense, we constructed the volcano plots with the r and average EN of IMC as the reactivity descriptors (Figure 5).

In Figure 5, the broken lines represent the overpotentials predicted with the linear least square fits in Figures 3a and 4. At each reactivity descriptor (r or EN), ΔG_i of each step was calculated to determine the RDS as well as the overpotential; this also provided the RDS boundaries. (Here, all thermody-

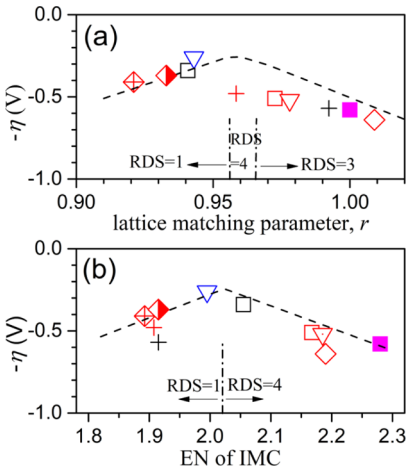

Figure 5. Overpotential (η) as a function of r (a) and average EN of IMC (b). The dashed lines show the overpotentials calculated with the fitted lines in Figures 3a and 4, respectively. The dashed lines break at the boundaries of RDSs whose domains are indicated with arrows.

https://dx.doi.org/10.1021/acs.jpcc.0c09674
J. Phys. Chem. C 2021, 125, 3527−3534

namic values other than the projected adsorption energies were those of Pt). Each broken line shows a peak representing the maximum ORR activity. In the plot of $-\eta$ versus r (Figure 5a), the peak is found at $r = 0.960 \pm 0.005$. The catalysts whose r is close to this value is Cu_3Ag@Pt (red cross). However, the $-\eta$ calculated directly with the adsorption energies is much lower. In the plot of $-\eta$ versus EN (Figure 5b), the peak is found at EN = 2.025 ± 0.005. The EN values of Cu_3Pt@Pt (blue reverse triangle) and FePt@Pt (black square) are close to this value, and the overall directly calculated plot symbols are much closer to the broken line. Yet, the directly calculated $-\eta$ values for CuAg@Pt (black cross) and $AgPt_3$@Pt (red diamond) are significantly off the broken line.

The two volcano plots shown in Figure 5 demonstrate that a single macroscopic parameter, whether it is r or average EN, is not a particularly good reactivity descriptor for the ORR process. Both the strain effect and the ligand effect influence the adsorption energies, although they are partially correlated; therefore, a parameter that combines both r an EN is considered. As a simple trial parameter, we tested a linear combination of r and EN: $(1 - a) \times \mathrm{EN}/2.28 + a \times r$. Here, 2.28 is the EN of Pt and a is a mixing coefficient. However, any single value of a failed to improve the linear fits significantly because the O-adsorption energies preferred a higher contribution of r, whereas the OOH- and OH-adsorption energies prefer a higher contribution of EN. Alternatively, we obtained the optimal a values to fit each of the adsorption energies (a = 0.38 for OOH, a = 0.83 for O, and a = 0.25 for OH-adsorption energies; this analysis is shown in the Supporting Information, Figure S5) and used them to calculate the overpotentials. The overpotentials (η_a) calculated in this way are tabulated in Table 2 to be compared with those (η_r and η_{EN}) calculated from the fitted adsorptions energies with r and EN. While η_r or η_{EN} show relatively large deviations for a few catalysts, η_a show evenly distributed deviations for all catalysts. As the result, the RMSD of η_a is lower than that of η_r or η_{EN}.

Table 2. Overpotentials (in V) Deduced from Different Fit Variables[a]

catalyst	η	η_r ($\delta\eta_r$)	η_{EN} ($\delta\eta_{EN}$)	η_a ($\delta\eta_a$)
Pt	0.58	0.57 (−0.01)	0.59 (0.01)	0.59 (0.01)
$FePt_3$@Pt	0.41	0.32 (−0.09)	0.44 (0.03)	0.43 (0.02)
FePt@Pt	0.34	0.34 (0.00)	0.29 (−0.05)	0.27 (−0.07)
Co_3Ag@Pt	0.41	0.45 (0.04)	0.43 (0.02)	0.46 (0.05)
$CuPt_3$@Pt	0.52	0.36 (−0.16)	0.46 (−0.06)	0.46 (−0.06)
Cu_3Pt@Pt	0.26	0.33 (0.07)	0.29 (0.03)	0.31 (0.05)
Cu_3Ag@Pt	0.48	0.25 (−0.23)	0.41 (−0.07)	0.46 (−0.02)
CuAg@Pt	0.57	0.45 (−0.12)	0.40 (−0.17)	0.55 (−0.02)
$AgPt_3$@Pt	0.64	0.56 (−0.08)	0.47 (−0.17)	0.57 (−0.07)
Ni_3Ag@Pt	0.37	0.38 (0.01)	0.40 (0.03)	0.41 (0.04)
RMSD		(0.08)	(0.06)	(0.04)

[a] η: calculated directly from computed adsorption energies, η_r, η_{EN}, η_a: calculated from fit adsorption energies with r, EN, $(1 - a) \times \mathrm{EN}/2.28 + a \times r$ as the dependent variable, respectively, and $\delta\eta_r$, $\delta\eta_{EN}$, $\delta\eta_a$: deviations from each η value.

Under our scheme, η_a is a function of r and EN, even though the functionality depends on the catalysts sampled and the quality of the linear fits. This motivated us to use r and EN as independent reactivity descriptors for the ORR efficiency, even though they are partly correlated. In Figure 6a, η_a is displayed as a two-dimensional contour map. The three blue broken lines represent the boundaries of the RDS. The highest ORR activity, or the minimum η_a, is found at a point where the three boundary lines meet. The coordinate of this point is (0.96, 2.025), which is consistent with the r and EN values at the volcano peaks of Figure 5.

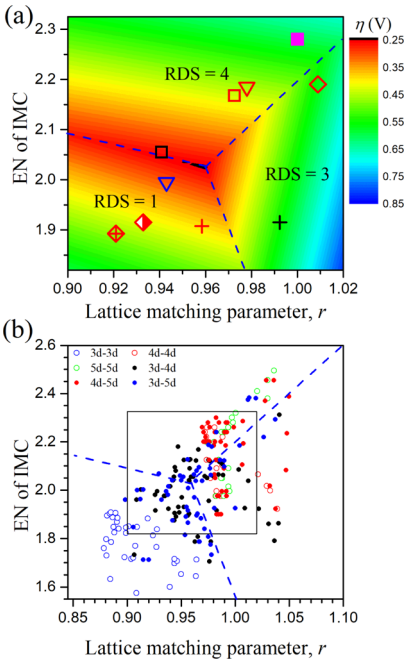

Figure 6. 2D volcano plot as a function of r and the average EN as dual reactivity descriptors. In (a), the contour map of overpotential (η_a) derived from the fits with $(1 - a) \times \mathrm{EN}/2.28 + a \times r$ is displayed and the (r, EN) coordinates of 10 catalysts in this work are overlaid. The plot symbols are described in Scheme 1. In (b), the coordinates of the IMCs with an extended list of transition metal elements are displaced. The rectangle in the middle of (b) represents the axes of (a).

The (r, EN) coordinates of the 10 IMCs in this work are plotted on the contour map of Figure 6a. The coordinates appear to follow a linear trend with the exception of CuAg (black cross). The rather big errors in fitting the adsorption energies of CuAg in Figures 3 and 4 are related to the large deviation of its coordinate from the general trend. With an interest in the coordinates for an extended list of IMCs, we obtained r and EN values for 241 IMCs whose optimized structures were found in the Materials Project,[29] which can accommodate a Pt(111) layer (shown in Table S7). Their coordinates are shown in Figure 6b in expanded axes. Figure 6b shows that IMCs with larger r values tend to have larger EN values. However, the coordinates shown in Figure 6b are more scattered from the linear trend than the coordinates of the 10 IMCs in Figure 6a.

There were 36 IMCs made of two 3d transition metal elements (blue open circles) in the extended list. However, only four of them had r values less than 0.90 and are expected to be unstable upon accommodating a Pt skin layer. Most IMCs made of two 4d transition metal elements (red open circles) and two 5d transition metal elements (green open circles) have r values between 0.98 and 1.00 with more or less widely spread EN values. The coordinates of these IMCs are far from the volcano peak. The coordinate region close to the volcano peak is occupied by the IMCs made by combining one

https://dx.doi.org/10.1021/acs.jpcc.0c09674
J. Phys. Chem. C 2021, 125, 3527−3534

3d element and one 4d or 5d element. If we limit the active region to 0.96 ± 0.01 for r and 2.025 ± 0.050 for EN, 11 IMCs belong to this group; they are VRu_3, VIr_3, $CrIr_3$, CrPt, $MnOs_3$, $MnIr_3$, Fe_3Au, CoPd, CoOs, NiPd, and NiIr.

CONCLUSIONS

In this study, we focused on the lattice matching parameter r and the average EN to quantify the strain effect and the ligand effect, respectively, as reactivity descriptors for the adsorption properties of Pt skin IMC (IMC@Pt) catalysts. The stable IMC@Pt should have r values between 0.90 and 1.0. Ten such candidate structures were selected to study the adsorption properties of intermediates of the ORR process.

The adsorption energies are correlated with both r and EN. However, in detailed analysis, the O-adsorption energies fit better with r, while the OOH- and OH-adsorption energies fit better with EN, implying that the strain effect and the ligand effect differently influence the O-adsorption and OOH- or OH-adsorptions. Therefore, instead of using either r or EN as a single parameter, we used both as descriptors. The overpotentials deduced this way were displayed as a contour map with r and EN as the dual reactivity descriptors. A volcano peak was found at the (r, EN) coordinate of (0.96, 2.025). When the coordinates of an extended list of the IMCs were overlaid on the contour map, we were able to identify 11 IMCs close to the volcano peak. This kind of analysis could be useful for a rapid screening of IMCs for high ORR activity because r and EN are easily obtained, while other reactivity descriptors demand accurate calculations.

ASSOCIATED CONTENT

Supporting Information

The Supporting Information is available free of charge at https://pubs.acs.org/doi/10.1021/acs.jpcc.0c09674.

> Input parameters for VASP; IMC@Pt slabs and their structures; adsorption sites and their adsorption energy data; fits with r and EN; and free energy change over the four steps of the ORR process (PDF)

AUTHOR INFORMATION

Corresponding Author

Graeme Henkelman − *Department of Chemistry and the Oden Institute for Computational Engineering and Science, The University of Texas at Austin, Austin, Texas 78712-1224, United States;* orcid.org/0000-0002-0336-7153; Email: henkelman@utexas.edu

Authors

Seong Kyu Kim − *Department of Chemistry, Sungkyunkwan University, Suwon 16419, Korea;* orcid.org/0000-0003-0902-3738

Kihyun Shin − *Department of Chemistry and the Oden Institute for Computational Engineering and Science, The University of Texas at Austin, Austin, Texas 78712-1224, United States;* orcid.org/0000-0002-1748-8773

Complete contact information is available at: https://pubs.acs.org/10.1021/acs.jpcc.0c09674

Notes

The authors declare no competing financial interest.

ACKNOWLEDGMENTS

The computational work at UT Austin was supported by the Welch Foundation (F-1841), the Department of Energy (DE-SC0010576) and with computational resources from the Texas Advanced Computing Center, the National Energy Research Scientific Computing Center, and the XSEDE program. This research was accomplished during a sabbatical in 2019 for S.K.K.

REFERENCES

(1) Zhu, J.; Hu, L.; Zhao, P.; Lee, L. Y. S.; Wong, K.-Y. Recent Advances in Electrocatalytic Hydrogen Evolution Using Nanoparticles. *Chem. Rev.* **2020**, *120*, 851−918.

(2) Ledezma-Yanez, I.; Wallace, W. D. Z.; Sebastián-Pascual, P.; Climent, V.; Feliu, J. M.; Koper, M. T. M. Interfacial Water Reorganization as a PH-dependent Descriptor of the Hydrogen Evolution Rate on Platinum Electrodes. *Nat. Energy* **2017**, *2*, 17031.

(3) Durst, J.; Simon, C.; Hasché, F.; Gasteiger, H. A. Hydrogen Oxidation and Evolution Reaction Kinetics on Carbon Supported Pt, Ir, Rh, and Pd Electrocatalysts in Acidic Media. *J. Electrochem. Soc.* **2015**, *162*, F190−F203.

(4) Davydova, E. S.; Mukerjee, S.; Jaouen, F.; Dekel, D. R. Electrocatalysts for Hydrogen Oxidation Reaction in Alkaline Electrolytes. *ACS Catal.* **2018**, *8*, 6665−6690.

(5) Shao, M.; Chang, Q.; Dodelet, J.-P.; Chenitz, R. Recent Advances in Electrocatalysts for Oxygen Reduction Reaction. *Chem. Rev.* **2016**, *116*, 3594−3657.

(6) Tang, Z.; Wu, W.; Wang, K. Oxygen Reduction Reaction Catalyzed by Noble Metal Clusters. *Catalysts* **2018**, *8*, 65.

(7) Kulkarni, A.; Siahrostami, S.; Patel, A.; Nørskov, J. K. Understanding Catalytic Activity Trends in the Oxygen Reduction Reaction. *Chem. Rev.* **2018**, *118*, 2302−2312.

(8) Hong, W. T.; Risch, M.; Stoerzinger, K. A.; Grimaud, A.; Suntivich, J.; Shao-Horn, Y. Toward the Rational Design of Non-precious Transition Metal Oxides for Oxygen Electrocatalysis. *Energy Environ. Sci.* **2015**, *8*, 1404−1427.

(9) Browne, M. P.; Sofer, Z.; Pumera, M. Layered and Two Dimensional Metal Oxides for Electrochemical Energy Conversion. *Energy Environ. Sci.* **2019**, *12*, 41−58.

(10) Zhong, Y.; Xia, X.; Shi, F.; Zhan, J.; Tu, J.; Fan, H. J. Transition Metal Carbides and Nitrides in Energy Storage and Conversion. *Adv. Sci.* **2016**, *3*, 1500286.

(11) Greeley, J.; Nørskov, J. K. Combinatorial Density Functional Theory-Based Screening of Surface Alloys for the Oxygen Reduction Reaction. *J. Phys. Chem. C* **2009**, *113*, 4932−4939.

(12) Fu, C.; Liu, C.; Li, T.; Zhang, X.; Wang, F.; Yang, J.; Jiang, Y.; Cui, P.; Li, H. DFT Calculations: A Powerful Tool for Better Understanding of Electrocatalytic Oxygen Reduction Reactions on Pt-based Metallic Catalysts. *Comput. Mater. Sci.* **2019**, *170*, 109202.

(13) Galyamova, A.; Shin, K.; Henkelman, G.; Crooks, R. M. Effect of TiO_x Substrate Interactions on the Electrocatalytic Oxygen Reduction Reaction at Au Nanoparticles. *J. Phys. Chem. C* **2020**, *124*, 10045−10056.

(14) Gamler, J. T. L.; Shin, K.; Ashberry, H. M.; Chen, Y.; Bueno, S. L. A.; Tang, Y.; Henkelman, G.; Skrabalak, S. E. Intermetallic Pd_3Pb Nanocubes with High Selectivity for the 4-Electron Oxygen Reduction Reaction Pathway. *Nanoscale* **2020**, *12*, 2532−2541.

(15) Mavrikakis, M.; Hammer, B.; Nørskov, J. K. Effect of Strain on the Reactivity of Metal Surfaces. *Phys. Rev. Lett.* **1998**, *81*, 2819−2822.

(16) Kattel, S.; Wang, G. Beneficial Compressive Strain for Oxygen Reduction Reaction on Pt (111) Surface. *J. Chem. Phys.* **2014**, *141*, 124713.

(17) Li, L.; Abild-Pedersen, F.; Greeley, J.; Nørskov, J. K. Surface Tension Effects on the Reactivity of Metal Nanoparticles. *J. Phys. Chem. Lett.* **2015**, *6*, 3797−3801.

(18) Zhang, X.; Xia, Z.; Li, H.; Yu, S.; Wang, S.; Sun, G. Theoretical Study of the Strain Effect on the Oxygen Reduction Reaction Activity and Stability of FeNC Catalyst. *New J. Chem.* **2020**, *44*, 6818−6824.

(19) Liu, M.; Xin, H.; Wu, Q. Unusual Strain Effect of a Pt-based $L1_0$ Face-centered Tetragonal Core in Core/shell Nanoparticles for the Oxygen Reduction Reaction. *Phys. Chem. Chem. Phys.* **2019**, *21*, 6477−6484.
(20) Kitchin, J. R.; Nørskov, J. K.; Barteau, M. A.; Chen, J. G. Role of Strain and Ligand Effects in the Modification of the Electronic and Chemical Properties of Bimetallic Surfaces. *Phys. Rev. Lett.* **2004**, *93*, 156801.
(21) Jennings, P. C.; Lysgaard, S.; Hansen, H. A.; Vegge, T. Decoupling Strain and Ligand Effects in Ternary Nanoparticles for Improved ORR Electrocatalysis. *Phys. Chem. Chem. Phys.* **2016**, *18*, 24737−24745.
(22) Li, H.; Shin, K.; Henkelman, G. Effects of Ensembles, Ligand, and Strain on Adsorbate Binding to Alloy Surfaces. *J. Chem. Phys.* **2018**, *149*, 174705.
(23) Greeley, J.; Stephens, I. E. L.; Bondarenko, A. S.; Johansson, T. P.; Hansen, H. A.; Jaramillo, T. F.; Rossmeisl, J.; Chorkendorff, I.; Nørskov, J. K. Alloys of Platinum and Early Transition Metals as Oxygen Reduction Electrocatalysts. *Nat. Chem.* **2009**, *1*, 552−556.
(24) Yang, Z.; Wang, J.; Yu, X. The Adsorption, Diffusion and Dissociation of O_2 on Pt-skin $Pt_3Ni(1\ 1\ 1)$: A Density Functional Theory Study. *Chem. Phys. Lett.* **2010**, *499*, 83−88.
(25) Ma, Y.; Balbuena, P. B. Pt Surface Segregation in Bimetallic Pt_3M Alloys: A Density Functional Theory Study. *Surf. Sci.* **2008**, *602*, 107−113.
(26) Lide, D. R. Section 9, Molecular Structure and Spectroscopy; Electronegativity. *CRC Handbook of Chemistry and Physics*, 84th ed.; CRC Press: Boca Raton, Florida, 2003.
(27) Kresse, G.; Joubert, D. From Ultrasoft Pseudopotentials to the Projector Augmented-Wave Method. *Phys. Rev. B: Condens. Matter Mater. Phys.* **1999**, *59*, 1758−1775.
(28) Hammer, B.; Hansen, L. B.; Nørskov, J. K. Improved Adsorption Energetics within Density-Functional Theory using Revised Perdew-Burke-Ernzerhof Functionals. *Phys. Rev. B: Condens. Matter Mater. Phys.* **1999**, *59*, 7413−7421.
(29) Kresse, G.; Furthmüller, J. Efficient iterative schemes forab initiototal-energy calculations using a plane-wave basis set. *Phys. Rev. B: Condens. Matter Mater. Phys.* **1996**, *54*, 11169−11186.
(30) Jain, A.; Ong, S. P.; Hautier, G.; Chen, W.; Richards, W. D.; Dacek, S.; Cholia, S.; Gunter, D.; Skinner, D.; Ceder, G.; Persson, K. A. Commentary: The Materials Project: A Materials Genome Approach to Accelerating Materials Innovation. *APL Mater.* **2013**, *1*, 011002.
(31) Nørskov, J. K.; Rossmeisl, J.; Logadottir, A.; Lindqvist, L.; Kitchin, J. R.; Bligaard, T.; Jónsson, H. Origin of the Overpotential for Oxygen Reduction at a Fuel-Cell Cathode. *J. Phys. Chem. B* **2004**, *108*, 17886−17892.
(32) Rossmeisl, J.; Qu, Z.-W.; Zhu, H.; Kroes, G.-J.; Nørskov, J. K. Electrolysis of Water on Oxide Surfaces. *J. Electroanal. Chem.* **2007**, *607*, 83−89.
(33) Man, I. C.; Su, H. Y.; Calle-Vallejo, F.; Hansen, H. A.; Martínez, J. I.; Inoglu, N. G.; Kitchin, J.; Jaramillo, T. F.; Nørskov, J. K.; Rossmeisl, J. Universality in Oxygen Evolution Electrocatalysis on Oxide Surfaces. *ChemCatChem* **2011**, *3*, 1159−1165.
(34) Liu, S.; White, M. G.; Liu, P. Mechanism of Oxygen Reduction Reaction on Pt(111) in Alkaline Solution: Importance of Chemisorbed Water on Surface. *J. Phys. Chem. C* **2016**, *120*, 15288−15298.
(35) Tang, W.; Sanville, E.; Henkelman, G. A Grid-based Bader Analysis Algorithm Without Lattice Bias. *J. Phys.: Condens. Matter* **2009**, *21*, 084204.
(36) Jacobsen, K. W.; Norskov, J. K.; Puska, M. J. Interatomic Interactions in the Effective-Medium Theory. *Phys. Rev. B: Condens. Matter Mater. Phys.* **1987**, *35*, 7423−7442.
(37) Ruban, A.; Hammer, B.; Stoltze, P.; Skriver, H. L.; Nørskov, J. K. Surface electronic structure and reactivity of transition and noble metals1Communication presented at the First Francqui Colloquium, Brussels, 19-20 February 1996.1. *J. Mol. Catal. A: Chem.* **1997**, *115*, 421−429.
(38) Rossmeisl, J.; Karlberg, G. S.; Jaramillo, T.; Nørskov, J. K. Steady State Oxygen Reduction and Cyclic Voltammetry. *Faraday Discuss* **2008**, *140*, 337−346.

https://dx.doi.org/10.1021/acs.jpcc.0c09674
J. Phys. Chem. C 2021, 125, 3527−3534